

Version 4976R1 to: American Mineralogist August 11, 2014

Carbon speciation in silicate-C-O-H melt and fluid as a function of redox conditions: An experimental study, *in-situ* to 1.7 GPa and 900°C

Bjorn Mysen
Geophysical Laboratory
Carnegie Instn. Washington
USA

Abstract

Carbon speciation in and partitioning among silicate-saturated C-O-H fluids and (C-O-H)-saturated melts have been determined ~1.7 GPa and 900°C under reducing and oxidizing conditions. The measurements were conducted *in-situ* while the samples were at the conditions of interest. The solution equilibria were (1) $2CH_4+Q^n=2CH_3^-+H_2O+Q^{n+1}$ and (2) $2CO_3^{2-}+H_2O+2Q^{n+1}=HCO_3^-+2Q^n$, under reducing and oxidizing conditions, and where the superscript, *n*, in the Q^n-species denotes number of bridging oxygen in the silicate species (Q-species). The abunmdance ratios, CH_3/CH_4 and HCO_3^-/CO_3^{2-}, increase with temperature. The enthalpy change associated with the species transformation differs for fluids and melts and also for oxidized and reduced carbon (Reducing: $\Delta H_{(1)}^{fluid}$ = 16±5 kJ/mol, $\Delta H_{(1)}^{melt}$ = 50±5 kJ/mol; oxidizing $\Delta H_{(2)}^{fluid}$=81±14 kJ/mol). For the exchange equilibrium of CH_4 and CH_3 species between fluid and melt, the temperature-dependent equilibrium constant, $(X_{CH4}/X_{CH3})^{fluid}/(X_{CH4}/X_{CH3})^{melt}$, yields ΔH=34±3 kJ/mol.

Increased abundance ratios, CH_4/CH_3 and HCO_3^-/CO_3^{2-}, lead to increased polymerization of silicate+(C-O-H) melt. Because of such relations, melt transport properties (e.g., viscosity) and element partition coefficients between magmatic liquids, C-O-H fluids, and crystalline phases can vary by more than 100% with speciation changes of C-bearing volatiles upper mantle. These structure effects are more pronounced the higher the pressure and the more mafic the magma.

Keywords: Redox, COH volatiles, melt structure, melt properties, fluid structure

Introduction

In (C-O-H)-bearing magmatic systems in the Earth's interior, redox conditions affect physicochemical properties of melts, melting phase relations, and element partitioning between coexisting phases. For example, during partial melting of a (C-O-H)-bearing the upper mantle under reducing conditions (methane is stable) melts tend to silica enrichment compared with anhydrous melting (Eggler and Baker, 1982; Green *et al.*, 1987; Brey et al., 2006). Under oxidizing conditions, partial melts tend toward silica under-saturation (Eggler, 1976; Wyllie, 1984). This is because the redox state(s) of carbon affects its solubility and solution mechanism(s) in silicate melts. However, the solubility and solution mechanism(s) are not only redox-dependent, but also vary with silicate composition, temperature, and pressure (Brooker et al., 2001; Mysen et al., 2011; Guillot and Sator, 2011).

In order to characterize the structure and the relationships between structure and properties of magmatic liquids and C-O-H fluids at high pressure and temperature, the characterization must be conducted while the sample is at the pressure, temperature, and redox conditions of interest because the imposed conditions change during the quenching process thus causing structural changes of melt and fluid as these are cooled from experimental to ambient conditions before analysis. This goal can be reached by containing the sample in externally heated diamond anvil cells and by using vibrational

spectroscopic methods to determine structural relationships. Results from such examination are provided in this report.

Experimental Methods

The (C-O-H)-free starting material was a glass of composition, $(Na_2Si_4O_9)_{90}$•$(Na_2(NaAl)_4O_9)_{10}$, denoted NA10, to which was added (C-O-H) components prior each experimental series (see also below). The material is from the same glass as that originally used by Mysen (2007). The degree of polymerization, NBO/T, of NA10 melt is near 0.5 with Al/(Al+Si) = 0.1. Here, Na^+ charge-balances Al^{3+} in tetrahedral coordination.

The experiments were conducted *in-situ* with the samples at the temperature, pressure, and redox conditions of interest by using an externally heated hydrothermal diamond anvil cell (HDAC) (Bassett *et al.*, 1994). In experiments under reducing conditions, Re gaskets was used for sample containment. Iridium gaskets were used for experiments under oxidizing conditions because under these conditions Re from the gasket reacts with H_2O and silicate to form rhenate complexes and H_2. Iridium is inert under the experimental conditions. The gaskets were 125 μm thick with a 500 μm central hole before experiments. During an experiment, the sample hole shrank to about 400 μm diameter with the gasket thickness between the two diamonds reduced to ~80-100 μm.

For experiments conducted under reducing conditions, NA10 glass starting glass was saturated with CH_4 prior to an experimental series in the HDAC. This methane-saturation was accomplished in a solid-media, high-pressure apparatus (Boyd and England, 1960) by equilibrating NA10 melt with C-O-H fluid at 1.5 GPa and 1400°C and at a hydrogen fugacity, f_{H2}, controlled by the reaction, $Mo+H_2O=MoO_2+H_2$. This equilibrium is within ~0.5 orders of magnitude of that of the often-used iron-wüstite buffer in the temperature-range of the present experiments (Mysen and Yamashita, 2010). The source of carbon was $Ag_2C_2O_4$, which decomposes to Ag and CO_2 at <200°C (Boettcher *et al.*, 1973). During high-temperature/-pressure synthesis this CO_2 reacts with the H_2 generated by the Mo/MoO_2 buffer reaction to yield CH_4 and H_2O ($CO_2 + 3H_2 = CH_4 + H_2O$). The melt was temperature-quenched to glass while at 1.5 GPa. The glass resulting from this procedure contains 0.74 wt% CH_4 (analyzed with an Elemental Analyzer as described by Mysen *et al.*, 2009). The glass also contains H_2O and H_2. For experiments in the HDAC under reducing conditions, this CH_4-bearing NA10 glass was loaded into the Re gasket hole together with Mo metal for the f_{H2} control, Pt metal for enhanced equilibration rate (Horita, 1988), carbon-13 synthetic diamond for pressure measurement (Mysen and Yamashita, 2010), and liquid H_2O. The Mo reacts with H_2O at a few hundred degrees C to form MoO_2 (Fig. 1) thus buffering the f_{O2} and f_{H2} during the experiments so that methane does not get oxidized.

In experiments under oxidizing conditions, volatile-free NA10 glass powder was loaded into the diamond cell together with $Ag_2C_2O_4$, Pt metal,

This is a preprint, the final version is subject to change, of the American Mineralogist (MSA)
Cite as Authors (Year) Title. American Mineralogist, in press.
(DOI will not work until issue is live.) DOI: http://dx.doi.org/10.2138/am-2015-4976CCBYNC

liquid H_2O, and synthetic carbon-13 diamond. Platinum was employed to enhance reaction rates (Horita, 1988). The silver oxalate decomposes to CO_2 and metallic Ag at <200°C.

Textural and structural characterization of the sample *in-situ* while at the redox conditions, temperatures, and pressures of interest was carried out with optical microscopy and Raman spectroscopy. The Raman spectrometer was a JASCO model NRS-3100 confocal microRaman system equipped with a single monochromator, a holographic notch filter, and holographic gratings. This system was used with 532 and 490 nm solid-state lasers for sample excitation with about 7 mW and 30 mW power at the sample, respectively. A 50X Mitutoyo™ long working distance objective (2.5 cm working distance, 0.42 N.A.) was used for optical monitoring and signal collection. The signal was recorded with an Andor™ Model DV401-F1 1024x128 pixel (25 μm pixel size) Peltier-cooled CCD.

The confocal optics in the Raman system restricts the sample depth excited by the laser. There is, nevertheless, a finite depth within which the laser produces a Raman signal. This depth can be an issue in the present experiments because during experiments under reducing conditions 10-30 μm diameter spheres of transparent melt rest on the bottom diamond culet, but otherwise are surrounded by transparent fluid. To evaluate the extent to which such an environment may lead to signal interference from fluid on the signal from melt, Raman intensity from a clear glass sample in contact with air was used as a model of the optical environment. The Raman signal intensity

decreases by about 90% within 25 μm of the focal plane (Fig. 2). As 30μm melt spheres were analyzed during the experiments, ≥ 90% of the signal is from the melt sphere, but with some interference from the surrounding fluids. The effect on the uncertainty in the experimental data of this environment is discussed further below.

The groove density of the holographic gratings governs the frequency resolution of the spectrometer. For most sample measurements (melt and fluid), 600 grooves/mm were used, which results in ±4 cm^{-1} frequency uncertainty. With 600 grooves/mm, the width of a single CCD window is ~3900 cm^{-1} in the frequency range of the present experiments. With 1200 and 2400 grooves/mm, the uncertainties were ±2 and ±1 $^{cm-1}$ and window widths of about 1900 and 1000 cm^{-1}, respectively. These higher groove-density gratings were employed when better frequency precision was needed.

Temperature was measured with two K-type thermocouples touching the upper and lower diamonds, respectively, and located less than 1 mm from the sample itself. With this configuration, the temperature uncertainty is ±2°C (Mibe *et al.*, 2008). Pressure was measured with the frequency of the one-phonon Raman peak of carbon-13 diamond (at known temperature; see also Schiferl *et al.*, 1997). For these latter measurements, 2400 grooves/mm were employed. A spectrum of some of the Ne emission lines was recorded simultaneously with the one-phonon vibration from carbon-13 diamond in order to improve on the frequency uncertainty in these measurements. By correcting the one-phonon Raman shift with the aid of the Ne emission lines a ±0.1 cm^{-1}

This is a preprint, the final version is subject to change, of the American Mineralogist (MSA)
Cite as Authors (Year) Title. American Mineralogist, in press.
(DOI will not work until issue is live.) DOI: http://dx.doi.org/10.2138/am-2015-4976CCBYNC

frequency uncertainty was achieved. This frequency uncertainty corresponds to a contribution of ±40°C to the total pressure. The calibration of the pressure/temperature effect on the one-phonon Raman band of ^{13}C diamond adds to the pressure uncertainty (±100 MPa; Mysen and Yamashita, 2010). These two contributions result in an overall pressure uncertainty of ±110 MPa. This uncertainty is independent of pressure because its contributions are from the fitting error of the data used in the pressure calibration and from the fixed uncertainty of the spectrometer reading.

Platinum was used to enhance equilibration rate (Horita, 1988). Results from time studies in the system NA10+H_2O+D_2O in similar temperature and pressure ranges indicated that D/H equilibrium was reached in minutes (Mysen, 2013). As chemical equilibration occurs on a faster time-scale than isotope equilibration, 1-hour dwell time prior to a measurement is, therefore, considered sufficient to reach equilibrium in the current experiments.

Results

Each experimental temperature/pressure path was started at the highest planned temperature and pressure for the first measurements followed by decreasing temperature and pressure (Fig. 3). The samples remained at each temperature and pressure condition for about 1 hour before spectra were recorded. The cooling rate between measurements was 100°C/min.

In experiments under reducing conditions the initial step was to bring the sample to 850°C/1446 MPa (see also Fig. 3). At this condition, there is a

single supercritical fluid containing silicate components, CH_4, H_2, and H_2O. The Raman spectrum of this fluid was then recorded and followed by measurements of supercritical fluid at 800°C/1419 MPa and 725°C/1119 MPa. Upon further cooling, to near 700°C/~1000 MPa, separation occurs into (C-O-H)-rich, silicate-saturated fluid and (C-O-H)-saturated silicate melt. The first measurements of coexisting fluid at melt were carried out at 675°C/986 MPa followed by 50°C temperature decrements between each set of spectroscopic measurements until the glass transition temperature was approached. The glass transition temperature is not accurately known, but is less than about 430°C (the glass transition temperature of anhydrous Al-free NS4; see also Knoche *et al.*, 1994). The presence of Al and H_2O likely will cause a lowering of this temperature so 425°C/492 MPa was chosen as the lowest pressure and temperature conditions for measurements of supercooled liquid and coexisting fluid under reducing conditions.

In experiments under oxidizing conditions, the sample initially was brought to 900°C/1745MPa (the highest temperature and pressure in these experiments) where a supercritical silicate+H_2O+CO_2 fluid exists together with Ag metal. The sample was kept at this condition for about 1 hour to allow physical separation of the heavy Ag metal from the much less dense supercritical silicate+CO_2+H_2O supercritical fluid. The initial spectroscopic measurements then were carried out at this temperature and pressure (00°C/1745 MPa). Temperature and pressure were then decreased. Spectroscopic measurements of supercritical fluids were carried out at

This is a preprint, the final version is subject to change, of the American Mineralogist (MSA)
Cite as Authors (Year) Title. American Mineralogist, in press.
(DOI will not work until issue is live.) DOI: http://dx.doi.org/10.2138/am-2015-4976CCBYNC

T>800°C and >1427 MPa and of coexisting fluids and melts from 800°C/1427 MPa to 610°C/1015 MPa at the temperature and pressure intervals shown in Fig. 3. The last measurements were at 610°C/1015 MPa because carbonate minerals crystallize from the melt+fluid assemblage at temperatures between 600° and 575°C (Fig. 4).

Raman spectroscopy

In the frequency range between ~400 and ~1200 cm^{-1} Raman signals occur that are assigned to (Si,Al)-O vibrations. In addition, C-O vibrations from molecular CO_2, HCO_3, and CO_3 groups also can be found in this frequency range. The 2800-4200 cm^{-1} frequency range comprises that where the most intense Raman bands assigned to C-H, O-H, and H-H stretch vibrations are located.

Oxidizing Conditions. In the 400-1200 cm^{-1} region, spectra of melt are dominated by three broad intensity maxima near 520, 900 and 1100 cm^{-1}, respectively (Fig. 6A). Additional bands or shoulders occur between 520 and 900 cm^{-1}. In the spectra of (CO_2+H_2O) fluid, the Raman intensities near 520 and 900 cm^{-1} are greatly reduced or not detected at all (Fig. 6A). A sharper band centered near 1050 cm^{-1} has replaced the broad 1100 cm^{-1} band seen in this frequency region of the melt spectra. The dominant band in the spectra of fluid, however, is that near 780 cm^{-1} (Fig. 6A). The differences between spectra of fluid and coexisting melt are highlighted further in the difference spectra (Fig.

This is a preprint, the final version is subject to change, of the American Mineralogist (MSA)
Cite as Authors (Year) Title. American Mineralogist, in press.
(DOI will not work until issue is live.) DOI: http://dx.doi.org/10.2138/am-2015-4976CCBYNC

7). Here, a spectrum of melt is subtracted from that of coexisting fluid (Fig. 7). In the difference spectra, the dominant intensity is near 780 cm^1 together with less intense maxima near 670 cm^{-1}, 970 cm^{-1} and 1050 cm^{-1}. The pronounced negative difference near 520 cm^{-1} reflects the lack of intensity in this region of spectra of fluid.

The low-frequency region (~400-~1200 cm^{-1}) was fitted to lines of Gaussian shape as illustrated with a few examples in Fig. 8. In fitting these spectra, statistical treatment (χ^2 minimization) was augmented with existing information on speciation in hydrous melts and fluids in the NA10+H_2O system (Mysen, 2010a). Assignments were guided by literature data as reviewed, for example, by Mysen and Richet (2005). In spectra of melt and supercritical fluids (Fig. 8) the 1100, 860, 820, and 775 cm^{-1} bands are assigned to (Si,Al)-O^- stretch vibrations in Q^3, Q^2, Q^1, and Q^0 silicate structural units, respectively (O^- indicates nonbridging oxygen. The superscript in the Q^n-notation indicates number of bridging oxygen in the structural entity). In some spectra of melts, a very weak signal near 1150 cm^{-1} may be assigned to (Si,Al)-O^o vibrations in Q^4 species. In spectra of melts, there is also a strong 510 and a distinct 580 cm^{-1} band, which are assigned to (Si.Al)-O-(Si,Al) bending or rocking motions in structural units with bridging oxygen (the possible structural units with bridging oxygen are Q^1, Q^2, Q^3, and Q^4). Bands at 860 and 820 cm^{-1} also are observed in the spectra of fluids, but are considerable weaker than in the melt spectra. The dominant band in spectra of fluids is that fitted near 775 cm^{-1}.

In the 400-1200 cm^{-1} frequency region, there can be as many as four bands that are not observed in spectra of C-free samples (grey-filled bands marked "a", "b", "c", and "d" in the examples in Fig. 8). In general, these bands are most intense in the spectra of fluid and least intense in spectra of melt. The highest-frequency band, between 1040 and 1070 cm^{-1} ("d"), occurs in all spectra. A strong Raman band near this frequency is always is present in spectra of CO_2-rich silicate glasses and melts, and is assigned to symmetric C-O stretching in CO_3 groups (e.g., Fine and Stolper, 1986; Brooker *et al.*, 2001). In the spectra of high-temperature/pressure fluid and supercritical fluid, a band marked "c" occurs slightly below 1000 cm^{-1}. It is assigned to C-OH stretching in HCO_3 groups (e.g., Frantz, 1998). The band near 670 cm^{-1} ("b" in Fig. 6) could be a bending mode in either CO_2, CO_3 or HCO_3 groups, or combinations of these (Davis and Oliver, 1972). Contributions to this intensity from CO_3 and HCO_3 groups are likely given the structural interpretation of the Raman bands in the 1000-1070 cm^{-1} region immediately above. A contribution from molecular CO_2 is possible because solution of a portion of carbon dioxide in silicate melts in the form of molecular CO_2 is common (Fine and Stolper, 1986; Nowak *et al.*, 2003). Unfortunately, the characteristic Fermi doublet from molecular CO_2, near 1280 and 1380 cm^{-1} (Colthup *et al.*, 1975) cannot be observed in the present spectra because this frequency region is within the frequency-range of the very strong one-phonon Raman band from diamond in the diamond cell. It is not possible, therefore, to include or exclude the presence of CO_2 from the Raman data. Finally, a fourth

band, near 620 cm^{-1} ("a"), occurs in spectra of melts and fluids (Fig. 8). This band is assigned to a C-OH bending motion in the HCO_3 groups (Davis and Oliver, 1972; Frantz, 1998). This band may also exist in spectra of supercritical fluid, but lack of spectral resolution in the frequency region near 600 cm^{-1} at the high temperature of supercritical fluid makes such a band unresolvable (Fig. 8).

The higher-frequency range of spectra recorded under oxidizing conditions, between about 2900 and 4200 cm^{-1}, comprises a single band centered near 3550 cm^{-1} (Fig. 6C). Its full width at half height, FWHH, decreases with increasing temperature (see insert in Fig. 6C), resembling the temperature evolution of this band in Raman spectra of other hydrous silicate glasses and melts and of aqueous fluids (e.g., Kawamoto *et al.*, 2004; Ratcliffe and Irish, 1982; Mysen, 2010a,b). The 3550 cm^{-1} band becomes increasingly asymmetric with decreasing temperature, which is also similar to that of H_2O dissolved in other silicate melts at high temperature and pressure as well as a pure H_2O fluid (Frantz *et al.*, 1993; Kawamoto et al., 2004; Mysen, 2010b). The Raman bands in this envelope are assigned to OH stretching, whether in OH groups forming metal-OH bonding or as a part of molecular H_2O. The asymmetry as this Raman band, seen the most clearly at low temperature, is consistent with more than one type of OH-groups and with increasing extent of hydrogen bonding with decreasing temperature (Mysen and Virgo, 1986; Walrafen *et al.*, 2002).

This is a preprint, the final version is subject to change, of the American Mineralogist (MSA)
Cite as Authors (Year) Title. American Mineralogist, in press.
(DOI will not work until issue is live.) DOI: http://dx.doi.org/10.2138/am-2015-4976CCBYNC

Reducing conditions. At the hydrogen fugacity of the Mo-MoO_2 buffer (reducing conditions), the low-frequency portion of spectra of fluid and melt is dominated by sharp bands near 880 and 900 cm^{-1} and by an intense, but broader, band near 300 cm^{-1} (Fig. 6B). There is also a weaker band near 780 cm^{-1} and a shoulder between 780 and 880 cm^{-1}. Also shown in Fig. 6B is a spectrum of crystalline MoO_2 recorded at ambient temperature and pressure. This MoO_2 spectrum shows major sharp peaks near the main peaks of spectra of melts and fluids in this frequency range. In light of the observation of finely disseminated MoO_2 through the sample (Fig. 1), we conclude that this portion of the Raman spectrum is dominated by Mo-O vibrations from the crystalline MoO_2 needles (Busey and Keller, 1964). These very strong Raman bands make band assignments and interpretation of silicate structure from the spectroscopic information in this frequency region difficult, which, therefore, was not attempted.

The higher-frequency spectral range, between about 2800 and 4200 cm^{-1}, is where Raman bands can occur that would be assigned to C-H (near 2900 cm^{-1}), O-H (centered near 3550 cm^{-1}), and H-H (near 4100 cm^{-1}) stretch vibrations, respectively. These vibrations would occur because the samples comprised hydrocarbon functional groups (e.g., CH_4), in H_2O (and OH), and in H_2 molecules (Walrafen, 1964; Nakamoto, 1978; Chou *et al.*, 1990). The most intense peak is centered near 3550 cm^{-1} (Fig. 6 D), similar to spectra from oxidizing conditions (Fig. 6C), and is assigned, therefore, to O-H stretching in

306 structurally bound OH groups and in molecular H_2O (Ratcliffe and Irish, 1982;
307 Walrafen *et al.*, 1986).

308 The sharp peak near 2900 cm^{-1} (Fig. 6D) is assigned to C-H stretching in
309 methane, in methyl groups, or both (Chou *et al.*, 1990; Socrates, 2002; Mysen
310 and Yamashita, 2010; Mysen *et al.*, 2011). This band is slightly asymmetric. The
311 extent of asymmetry in spectra of coexisting melts and fluids differs. This
312 difference is seen more clearly in difference spectra obtained by subtracting
313 spectra of melt from those of coexisting fluid at the same temperature and
314 pressure (Fig. 9). The asymmetry and intensity differences may exist because
315 the 2900 cm^{-1} band comprises more than one symmetric Raman band the
316 relative intensities of which differ in spectra of melts and fluids. Two peaks of
317 Lorentzian shape, near 2900 and 2915 cm^{-1}, result from curve-fitting of the
318 spectra (Fig. 10), perhaps assignable to C-H stretching in two (C-H)-bearing
319 groups in the melts and fluids. That suggestion is consistent with a recent
320 carbon-13 MAS NMR study of (C-O-H)-saturated NA10 glass that was formed
321 by temperature-quenching (from 1400°C) of melt at 1.5 GPa (Mysen *et al.*,
322 2011). In that study, the precursor melts was equilibrated with C-O-H fluid at
323 the f_{H2} of the iron-wüstite buffer before quenching to glass. Both CH_4 and CH_3
324 groups were detected in the NMR spectra of this glass (see Fig. 11). Given the
325 same silicate composition and quite similar hydrogen fugacity in the present
326 experiments and those of the ^{13}C NMR study by Mysen et al. (2011) (see also
327 Fig. 11), it is concluded that the two peaks fitted to the 2900 cm^{-1} Raman band
328 in the spectra of reduced silicate-C-O-H melts and fluids (figs. 9 and 10) should

be assigned to C-H stretching in molecular CH_4 and in CH_3 groups. The 2915 cm^{-1} band assigned to C-H symmetric stretching in molecular CH_4 (Dubessy *et al.*, 1999). The peak near 2900cm^{-1} is assigned to C-H stretching in the CH_3 groups, which is consistent with that of symmetric C-H stretching in $Si(CH_3)_4$ (Nakamoto, 1978).

Finally, there is a sharp, but weak, band near 4120 cm^{-1} (see right insert in Fig. 6D). It is assigned to H-H stretching in H_2 molecules in the fluid and in the melt (e.g., Veirs and Rosenblatt, 1987).

Discussion

Concentration ratios of carbon species in fluids and melts and carbon species partitioning between them may be estimated from their Raman spectra. This is possible because the variables affecting the intensity of a Raman band assigned to a specific vibration in an amorphous material such as melt and fluid are concentration, temperature and Raman cross-sections (e.g., Long, 1977). For equilibria of carbon species between fluid and melt, density differences do not affect the Raman intensity and temperature cancels out in a simple ratio. Temperature effects on intensity ratios assigned to similar type of vibration also cancel out because the frequencies of the bands under study are so far from the laser excitation frequency that temperature- and frequency-dependent scattering intensity variations are within the background scatter of the data. In principle, there is a difference between these species (CH_4 versus CH_3 and CH_3 versus HCO_3) because the will be affected by next neighbors (ie, H

vs. Si). The size of this difference cannot be estimated. However, in analogy with Si-O stretching in SiO_4 tetrahedra with different number of bridging and nonbridging oxygen in silicate glasses where the scattering factors differ only be several percent, it is assumed that the cross sections are the same for symmetric C-H stretching in CH_3 and CH_4 groups and of the C-O stretching in CO_3 and HCO_3 groups, respectively. The ratio of integrated Raman intensities of bands assigned to similar vibrations in spectra of coexisting phases, a and b, or the ratio if different C-bearing species in a given phase then is related to the ratios of the relevant species, X_i, via the Raman cross section, α_i, so that a partition coefficient, $K_i^{a/b}$, is:

$$K_i^{a/b} = \frac{X_i^a}{X_i^b} = \frac{\alpha_i^b}{\alpha_i^a} \bullet \frac{A_i^a}{A_i^b}. \quad (1)$$

Solution mechanisms, oxidized carbon

The equilibrium between silicate structure (Q-species), H_2O, CO_3, and HCO_3 groups in fluid, supercritical fluid, and melt can be written as;

$$2CO_3^{2-} + H_2O + 2Q^{n+1} \rightleftharpoons 2HCO_3^- + 2Q^n, \quad (2)$$

with the equilibrium constant;

373 $$K_{(2)} = \left(\frac{X_{HCO_3^-}}{X_{CO_3^{2-}}}\right)^2 \cdot \left(\frac{X_{Q^n}}{X_{Q^{n+1}}}\right)^2 \cdot \frac{1}{f_{H_2O}}. \quad (2a)$$

374

375 In eqn. (2), the superscript in the Q^n-notation denotes the number of bridging
376 oxygen in the species, X_{Q^n}, and f_{H2O} is the fugacity of H_2O. In these and
377 subsequent expressions activity of Q-species species is assumed equal to mol
378 fraction.

379 For fluid and supercritical fluid, equilibrium (2) shifts to the left with
380 temperature as the $\frac{X_{HCO_3^-}}{X_{CO_3^{2-}}}$-ratio decreased from ~1.4 to ~0.2 (Fig. 12). This
381 temperature-dependence results in $\Delta H = 81 \pm 14$ kJ/mol (Table 1). The
382 abundance of HCO_3 groups in hydrous melts could not be estimated because of
383 the lack of spectral resolution in the spectra of melts near 1000 cm^{-1} so that an
384 enthalpy change associated with carbon speciation abundance changes could
385 not be determined either. Given the similar structural features of
386 silicate/carbonate in fluids, melts and supercritical fluid, a negative
387 temperature dependence seems likely for melts. It follows that the structure of
388 silicate dissolved in oxidized C-O-H fluid and in (C-O-H)-saturated silicate melt
389 becomes more polymerized with increasing temperature.

390

391 *Solution mechanisms, reduced carbon*

392 In the experiments conducted under reducing conditions, the melt spheres are
393 smaller than the distance between the two diamonds of the diamond cell (≤30

This is a preprint, the final version is subject to change, of the American Mineralogist (MSA)
Cite as Authors (Year) Title. American Mineralogist, in press.
(DOI will not work until issue is live.) DOI: http://dx.doi.org/10.2138/am-2015-4976CCBYNC

394 μm-diameter melt spheres and 80-100 μm distance between diamonds in
395 sample chamber, respectively). Some interference of the melt spectral
396 intensities from the adjoining fluid was, therefore, unavoidable. With the
397 confocal Raman system used here, about 90% of the signal recorded is from
398 melt with about a 10% contribution from adjoining fluid (see also Fig. 2 and
399 discussion above). This means that partition coefficients and Raman band
400 intensity ratios can be affected. The A_{2915}/A_{2900} is of particular interest as this
401 ratio expresses abundance ratio, CH_3/CH_4. With the A_{2915}/A_{2900} area ratios of
402 melts, which typically are between 2 and 3, a 10% contribution to the signal of
403 melt from adjoining fluid adds between 5 and 10% uncertainty to the
404 A_{2915}/A_{2900} area ratios. However, given that the melt sphere diameter does not
405 vary significantly with temperature (and pressure), this contribution to the
406 carbon partition coefficients for reduced carbon likely is not discernably
407 temperature-dependent.

408 For fluid and melt equilibrated with C-O-H fluid under reducing conditions
409 the solution equilibrium between Q-species (silicate structure), H_2O, CH_3-
410 groups, and CH_4 can be described as;
411

412 $$2CH_4 + Q^n \rightleftharpoons 2CH_3 + Q^{n+1} + H_2O, \quad (3)$$

413

414 with the equilibrium constant;
415

This is a preprint, the final version is subject to change, of the American Mineralogist (MSA)
Cite as Authors (Year) Title. American Mineralogist, in press.
(DOI will not work until issue is live.) DOI: http://dx.doi.org/10.2138/am-2015-4976CCBYNC

$$K_{(3)} = \left(\frac{X_{CH_3}}{X_{CH_4}}\right)^2 \cdot \left(\frac{X_{Q^{n+1}}}{X_{Q^n}}\right)^2 \cdot f_{H_2O}. \quad (3a)$$

Equation (3) shifts to the right with decreasing temperature and at a faster rate in melts than in coexisting fluid because the abundance ratio, $\frac{X_{CH_3}}{X_{CH_4}}$, in melt is more sensitive to temperature than in the fluid (Fig. 13). However, the $\frac{X_{CH_3}}{X_{CH_4}}$-values of melt are minimum values because of the interference problem associated with adjoining fluid (the $\frac{X_{CH_3}}{X_{CH_4}}$ of fluid is smaller than that of melt). However, the temperature trends are not affected by this uncertainty. The temperature-dependent trend implies that increasing temperature leads to depolymerization of the silicate network (Q^{n+1}/Q^n decreases and, therefore, NBO/T decreases).

By combining the C-H speciation data for coexisting fluid and melt, an exchange equilibrium can be written:

$$(CH_4)^{fluid} + (CH_3)^{melt} \rightleftharpoons (CH_4)^{melt} + (CH_3)^{fluid}, \quad (4)$$

with the exchange equilibrium coefficient;

$$K_{(4)} = \frac{(X_{CH_4} / X_{CH_3})^{fluid}}{(X_{CH_4} / X_{CH_3})^{melt}}. \quad (4a)$$

The temperature-dependence of this exchange coefficient (Fig. 13) yields $\Delta H = 34 \pm 3$ kJ/mol (Table 1). In other words, increasing temperature (and pressure) favors a fluid with molecular CH_4 coexisting with melt where the reduced carbon species are increasingly dominated by CH_3-groups. It is emphasized, however, that the errors of ΔH-values in Table 1 for equations (3) and (4) do not include the contribution from the fluid interference on the Raman spectra of melt. As discussed above (and see also Fig. 2) The signal from fluid interference on melt spectra introduces an additional 5-10% uncertainty in the ΔH-values over and beyond those listed in Table 1 and shown in the error bars in Figs. 13 and 14.

Implications

Recent experimental data on speciation of C-O-H volatiles in silicate melts as a function of redox conditions in the temperature/pressure range of the upper mantle indicate that reduced C-species such as CH_4 and CH_3 groups may be stable at oxygen fugacities, f_{O2}, near and below that corresponding to the magnetite-wüstite (MW) oxygen buffer (Mysen *et al.*, 2011). Oxidized carbon, as CO_2 or CO_3 groups, or both, dominate speciation in melts at higher f_{O2}. The f_{O2} of the present day upper mantle likely is within 1-2 orders of magnitude of MW (O'Neill, 1991; McCammon, 2005). It follows that methane and compositionally related functional groups (e.g., CH_3 groups in silicate melt

This is a preprint, the final version is subject to change, of the American Mineralogist (MSA)
Cite as Authors (Year) Title. American Mineralogist, in press.
(DOI will not work until issue is live.) DOI: http://dx.doi.org/10.2138/am-2015-4976CCBYNC

456 structure) might be more common in the present mantle than hitherto
457 assumed. An understanding the relationships between equilibria involving
458 both oxidized and reduced carbon species is necessary, therefore, to
459 characterize the carbon budget in the Earth and to understand how carbon
460 speciation in melts (magmatic liquids) governs physical and chemical
461 properties of magmatic systems in the Earth's interior.

462 Carbon species, whether oxidized or reduced, affect the degree of silicate
463 melt polymerization. The degree of silicate polymerization is often quantified
464 in terms of the proportion of nonbridging oxygen to tetrahedrally coordinated
465 cations, NBO/T. The degree of polymerization of silicate melt structure is an
466 important, but not the only, factor controlling melt properties. We note,
467 however, that abundance of Q^n-species and the value of NBO/T (nonbridging
468 oxygen per tetrahedrally coordinated cations) are linked via the expression;
469

470 $$NBO/T=\sum_{n=0}^{n=4} X_{Q^n} \cdot (NBO/T)_{Q^n}, \quad (5)$$

471

472 where NBO/T is the bulk melt NBO/T, and $(NBO/T)_{Q^n}$, that of individual Q^n-
473 species. The X_{Q^n} is the mol fraction of the individual Q^n-species.

474 Melt structure/property relations often are insufficiently well understood
475 to relate those to the behavior of individual Q^n-species. For the purpose of the
476 present discussion we will assess, therefore, only relationships to bulk melt
477 NBO/ where property-NBO/T relations are well established.

Melt viscosity and mineral/melt partition element coefficients are among the more important examples of melt properties that can be related nearly quantitatively to melt composition and, therefore, its polymerization. For example, viscosity data from a simple chemical system, Na_2O-SiO_2 at 1400°C (viscosity data from Bockris *et al.*, 1955), can be fitted to the NBO/T of the melt as (see also insert in Fig. 15);

$$\eta(\text{Pa s}) = 4.4 + 0.75 \bullet (\text{NBO}/\text{T})^{-4.1}. \quad (6)$$

From eqns. (2) and (3), the changes in melt polymerization, ΔNBO/T, CO_3/HCO_3 abundance ratio under oxidizing conditions and, CH_3/CH_4, under reducing conditions, respectively, are:

$$(\Delta\,\text{NBO}/\text{T})^{\text{oxidizing}} = 0.135 + 0.59 \bullet e^{(-0.55 \bullet (X_{CO_3}/X_{HCO_3}))} - 0.27 \bullet e^{(-2.3 \bullet (X_{CO_3}/X_{HCO_3}))}, \quad (7a)$$

and

$$(\Delta\,\text{NBO}/\text{T})^{\text{reducing}} = 0.135 + 0.59 \bullet e^{(-0.55 \bullet (X_{CH_3}/X_{CH_4}))} - 0.27 \bullet e^{(-2.3 \bullet (X_{CH_3}/X_{CH_4}))}. \quad (7b)$$

The change of melt viscosity, $\Delta\eta$, as a function of carbon speciation ratio in a melt is then calculated by combining eqns. (6) and (7) (Fig. 15). The effects are large (several hundred percent), but will depend on the NBO/T of the (C-O-H)-free melt because the viscosity versus NBO/T relationship is non-linear (See insert, Fig. 15).

Another example of how melt structure/composition can affect melt properties is the $Fe^{2+} \rightleftharpoons Mg$ exchange equilibrium between olivine and melt. This equilibrium often is used as an indicator of petrogenetic history of magmatic rocks in the Earth's interior with the assumption that an exchange equilibrium coefficient, $K_{D(Fe^{2+}-Mg)}^{olivine/melt} = (X_{Fe^{2+}} / X_{Mg})^{olivine} / (X_{Fe^{2+}} / X_{Mg})^{melt}$, is constant and equal to 0.3 [originally determined by Roeder and Emslie (1970)]. Subsequent experimental work has shown, however, that melt composition can affect the $K_{D(Fe^{2+}-Mg)}^{olivine/melt}$ by as much as about 50% (Walter and Kushiro, 1998; Kushiro and Mysen, 2002; Toplis, 2004). In an experimental study of $K_{D(Fe^{2+}-Mg)}^{olivine/melt}$ versus NBO/T of melts in the Na_2O-K_2O-CaO-MgO-FeO-Fe_2O_3-Al_2O_3-SiO_2 system, Kushiro and Mysen (2002), in accord with Kushiro and Walter (1998), found a parabolic relationship between $K_{D(Fe^{2+}-Mg)}^{olivine/melt}$ and NBO/T of the melt (see insert in Fig. 16). This relationship implies that the effect of carbon speciation ratio in melt on the direction of $K_{D(Fe^{2+}-Mg)}^{olivine/melt}$-change with carbon speciation ratio is different depending the NBO/T-value of the melt. For example, for a highly polymerized melt (NBO/T=0.25 is used in Fig. 16), increasing CH_3/CH_4 abundance ratio results in a negative change of $K_{D(Fe^{2+}-Mg)}^{olivine/melt}$. In contrast, in a highly depolymerized melt (NBO/T=2.25 is used in Fig. 16) the change of $K_{D(Fe^{2+}-Mg)}^{olivine/melt}$-values with increasing CH_3/CH_4 ratio is positive. Translated to NBO/T-values of melts of common igneous rocks, variation in carbon speciation in a magmatic liquid has different influence on $Fe^{2+} \rightleftharpoons Mg$

This is a preprint, the final version is subject to change, of the American Mineralogist (MSA)
Cite as Authors (Year) Title. American Mineralogist, in press.
(DOI will not work until issue is live.) DOI: http://dx.doi.org/10.2138/am-2015-4976CCBYNC

olivine/melt exchange equilibria for felsic melts compared with ultramafic melts.

Furthermore, from eqn. (2a) it follows that an increase in CO_3/HCO_3 abundance ratio leads depolymerization of the silicate structure (increased NBO/T), whereas from eqn. (3a) it follows that under reducing conditions, a decrease in abundance ratio, $\frac{X_{CH_3}}{X_{CH_4}}$, leads to increased abundance ratio, Q^{n+1}/Q^n, which means that the silicate melt becomes more polymerized. This contrasting behavior implies that $K_{D(Fe^{2+}-Mg)}^{olivine/melt}$ -changes with carbon speciation ratio also can vary with changes in redox conditions.

In the calculations shown in Figs. 15 and 16, the speciation ratio of carbon is treated as an independent variable. This ratio, whether oxidized or reduced depends on, temperature, pressure, melt composition and total carbon content in a melt. For example, with increasing temperature, eqns (2) and (3) shift to the left and right, respectively (Figs. 12 and 13). This means that under oxidizing conditions, increasing temperature results in silicate melt polymerization, whereas under reducing conditions, increasing temperature causes depolymerization of the silicate melt structure.

Carbon solubility, whether oxidized or reduced, increases with increasing pressure. This implies that the extent of melt polymerization change of a COH-bearing magmatic liquid in the mantle as a function of carbon speciation ratio also changes with pressure.

Finally, there is a positive correlation between carbon solubility itself and bulk melt NBO/T (Holloway et al., 1976; Brooker *et al.*, 2001). Basaltic magmatic liquids are likely, therefore, to be more sensitive to speciation variation than more felsic liquids (e.g., dacite and rhyolite) because the basalt is less polymerized (average NBO/T of rhyolite melt is near 0.1, whereas the average for basalt is around 0.9). These factors taken together illustrate the need to ascertain exactly how speciation of volatiles in magmatic liquids in the Earth's interior govern the physical and chemical properties of the magma.

Acknowledgments

This research was conducted with support from NSF grants EAR-1212754 and EAR-1250449. The solid-state 490 nm laser was acquired with funds provided by NSF grant EAR-1251931. A grant from the W. M. Keck Foundation supported acquisition of analytical instruments used in this study. A portion of this work was conducted while the author was visiting professor in GI^3 Lab (Global Intellectual Incubation and Integration Laboratory) program of WPI-AIMR (WPI-Advanced Institute for Materials Research), Tohoku University, in 2013. Their hospitality and assistance is greatly appreciated.

References

Bassett, W.A., Shen, A.H., Bucknum, M. and Chou, I.M. (1994) A new diamond cell for hydrothermal studies to 2.5 GPa and from -190°C to 1200°C. Reviews of Scientific Instruments 64, 2340-2345.

Bockris, J., O'M.Mackenzie, J.O. and Kitchner, J.A. (1955) Viscous flow in silica and binary liquid silicates. Transactions of the Faraday Society 51, 1734-1748.

Boettcher, A.L., Mysen, B.O. and Allen, J.C. (1973) Techniques for the control of water fugacity and oxygen fugacity for experimentatin in solid-media high-pressure apparatus. Journal of Geophysical Research 78, 5898-5902.

Boyd, F.R. and England, J.L. (1960) Apparatus for phase equilibrium measurements at pressures up to 50 kilobars and temperatures up to 1750°C. Journal of Geophysical Research 65, 741-748.

Brey, G.P., Bulatov, V.K. and Girnis, A.V. (2006) Redox melting and composition of near liquidus melts of C-O-H-bearing peridotite. Geochimica et Cosmochimica Acta 70, A67.

Brooker, R.A., Kohn, S.C., Holloway, J.R. and McMillan, P.F. (2001) Structural controls on the solubility of CO_2 in silicate melts Part I: bulk solubility data. Chemical Geology 174, 225-239.

Busey, R.H. and Keller, O.L. (1964) Structure of the Aqueous Pertechnetate Ion by Raman and Infrared Spectroscopy. Raman and Infrared Spectra of Crystalline $KTcO_4$, $KReO_4$, Na_2MoO_4, Na_2WO_4, $Na_2MoO_4{\cdot}2H_2O$, and $Na_2WO_4{\cdot}2H_2O$. Journal of Chemical Physics 41, 215-225.

Chou, I.-M., Pasteris, J.D. and Seitz, J.C. (1990) High density volatiles in the system C-O-H-N for the calibration of a laser Raman microprobe. Geochimica et Cosmochimica Acta Acta 54, 535-543.

Colthup, N.B., Daly, L.H. and Wiberley, S.E. (1975) Introduction to Infrared and Raman Spectroscopy. Academic Press.

Davis, A.R. and Oliver, B.G. (1972) A vibrational spectroscopic study of the species present in the CO_2-H_2O system. Journal of Solution Chemistry 1, 329-338.

Dubessy, J., Moissette, A., Bakker, R.J., Frantz, J.D. and Zhang, Y.-G. (1999) High-temperature Raman spectroscopic study of H_2O-CO_2-CH_4 mixtures in synthetic fluid inclusions: first insights on molecular interactions and analytical implications. European Journal of Mineralogy 11, 23-32.

Eggler, D.H., (1976) Does CO_2 cause partial melting in the low-velocity layer of the mantle? Geology 2, 69-72.

Eggler, D.H. and Baker, D.R. (1982) Reduced volatiles in the system C-H-O: Implications to mantle melting, fluid formation and diamond genesis. Advances in Earth and Planetary Science 12, 237-250.

Fine, G., and Stolper, E. (1986) Dissolved carbon dioxide in basaltic glasses: Concentration and speciation. Earth Planetary Science Letters 76, 263-278.

Frantz, J.D. (1998. Raman spectra of potassium carbonate and bicarbonate aqueous fluids at elevated temperatures and pressures: Compairson with theoretical simulations. Chemical Geology 152, 211-225.

Frantz, J.D., Dubessy, J. and Mysen, B. (1993) An optical cell for Raman spectroscopic studies of supercritical fluids and its applications to the study of water to 500°C and 2000 bar. Chemical Geology 106, 9-26.

Green, D.H., Falloon, T.J. and Taylor, W.R. (1987) Mantle-derived magma - roles of variable source peridotite and variable C-O-H fluid compositions. In: Mysen, B.O. (Ed.), Magmatic Processes: Physicochemical Principles. The Geochemical Society, University Park, Pennsylvania, pp. 139-154.

Guillot, B. and N. Sator, N. (2011) Carbon dioxide in silicate melts: A molecular dynamics simulation study. Geochimica et Cosmochimca Acta 75 1829-1857.

Holloway, J.R., Mysen, B. O. and Eggler, D. H. (1976) The solubility of CO_2 in liquids on the join CaO-MgO-SiO_2-CO_2. Carnegie Institution of Washington Yearbook 75, 626-631.

Horita, J. (1988) Hydrogen isotope analyses of natural waters using an H_2-water equilibration method: A special implication to brines. Chemical Geology 72, 89-94.

Jaeger, W.L. and Drake, M.J. (2000) Metal-silicate partitioning of Co, Ga, and W; dependence on silicate melt composition. Geochimica et Cosmochimica Acta 64, 3887-3895.

Kawamoto, T., Ochiai, S. and Kagi, H. (2004) Changes in the structure of water deduced from the pressure dependence of the Raman OH frequency. Journal of Chemical Physics 120, 5867-5870.

Knoche, R., Dingwell, D.B., Seifert, F.A. and Webb, S.L. (1994) Non-linear properties of supercooled liquids in the system Na_2O-SiO_2. Chemical Geology 116, 1-16.

Kushiro, I. (1976) A new furnace assembly with a small temperature gradient in solid-media, high-pressure apparatus. Carnegie Institution of Washington Year Book 75, 832-833.

Kushiro, I. and Walter, M. (1998) Mg-Fe Partitioning between olivine and mafic-ultramafic melts. Geophysical Research Letters 25, 2337-2340.

Kushiro, I. and Mysen, B.O. (2002) A possible effect of melt structure on the Mg-Fe2+ partitioning between olivine and melt. Geochimica et Cosmochimica Acta 66, 2267-2273.

Long, D.A. (1977) Raman Spectroscopy. McGraw-Hill, New York.

McCammon, C. (2005) Mantle oxidation state and oxygen fugacity: Constraints on mantle chemistry, structure and dynamics. In: van der Hilst, R.D., Bass, J.D., Matas, J., Trampert, J. (Eds.), Earth's Deep Mantle: Structure, Composition, and Evolution. American Geophysical Union, Washington D.C., pp. 221-242.

Mibe, K., Chou, I.M. and Bassett, W.A. (2008) In situ Raman spectroscopic investigation of the structure of subduction-zone fluids. Journal of Geophysial Research 1131-8.

Mysen, B.O. (2007) The solution behavior of H_2O in peralkaline aluminosilicate melts at high pressure with implications for properties of hydrous melts. Geochim. Cosmochim. Acta, 71, 1820-1834. Geochimica et Cosmochimica Acta 71, 1820-1834.

650 Mysen, B.O. (2010a) Structure of H_2O-saturated peralkaline aluminosilicate melt
651 and coexisting aluminosilicate-saturated aqueous fluid determined in-situ to
652 800°C and ~800 MPa. Geochimica et Cosmochimica Acta 74, 4123-4139.
653 Mysen, B.O. (2010b) Speciation and mixing behavor of silica-saturated aqueous
654 fluid at high temperature and pressure. American Mineralogist 95, 1807-1816.
655 Mysen, B.O. (2013) Hydrogen isotope fractionation between coexisting hydrous
656 melt and coexisting silicate-saturated aqueous fluid: An experimental study in-
657 situ at high pressure and temperature. American Mineralogist 98, 376-386.
658 Mysen, B.O., Fogel, M.L., Cody, G.D. and Morrill, P.L. (2009) Solution behavior
659 of reduced C-O-H volatiles in silicate melts at high pressure and temperature.
660 Geochimica et Cosmochimica Acta 73, 1696-1710.
661 Mysen, B.O., Kumamoto, K., Cody, G.D. and Fogel, M.L. (2011) Solubility and
662 solution mechanisms of C-O-H volatiles in silicate melt with variable redox
663 conditions and melt composition at upper mantle temperatures and pressures.
664 Geochimica et Cosmochimica Acta 75, 6183-6199.
665 Mysen, B.O. and Richet, P. (2005) Silicate Glasses and Melts - Properties and
666 Structure. Elsevier, New York, 564 pp.
667 Mysen, B.O. and Virgo, D., (1986) Volatiles in silicate melts at high pressure and
668 temperature. 1. Interaction between OH groups and Si^{4+}, Al^{3+}, Ca^{2+}, Na^{+} and H^{+}.
669 Chemical Geology 57, 303-331.
670 Mysen, B.O. and Yamashita, S. (2010) Speciation of reduced C-O-H volatiles in
671 coexisting fluids and silicate melts determined in-situ to ~1.4 GPa and 800°C.
672 Geochimica et Cosmochimica Acta 74, 4577-4588.
673 Nakamoto, K. (1978) Infrared and Raman spectra of inorganic and coordination
674 compounds. John Wiley & Sons, New York.
675 O'Neill, H.S.C. (1991) The origin of the Moon and the early history of the Earth - a
676 chemical model. Part 2: Geochimica et Cosmochimica Acta, 1159-1172.
677 Ratcliffe, C.I. and Irish, D.E. (1982) Vibrational studies of solutions at elevated
678 temperatures and pressures. 5. Raman studies of liquid water up to 300 °C.
679 Journal of Physical Chemistry 86, 4897-4905.
680 Roder, P.L. and Emslie, R.F. (1970) Olivine-liquid equilibrium. Contributions to
681 Mineralogy and Petrolology 29, 275-289.
682 Schiferl, D., Nicol, M., Zaug, J.M., Sharma, S.K., Cooney, T.F., Wang, S.-Y.,
683 Anthony, T.R. and Fleischer, J.F. (1997) The Diamond $^{13}C/^{12}C$ Isotope
684 Raman Pressure Sensor System for High Temperature/Pressure Diamond-
685 Anvil Cells with Reactive Samples. Journal of Applied Physics 82, 3256-3265.
686 Socrates, G. (2001) Infrared and Raman Characteristic Group Frequencies -
687 Tables and Charts. 3 ed. John Wiley & Sons, New York, 347pp.
688 Toplis, M.J. (2004) The thermodynamics of iron and magnesium partitioning
689 between olivine and liquid: Criteria for assessing and predicting equilibrium
690 in natural and experimental systems. Contributions to Mineralogy and
691 Petrology 149, 22-39.
692 Veirs, D.K. and Rosenblatt (G.M., 1987) Raman line positions in molecular
693 hydrogen - H_2, HD, HT, D_2, DT, and T_2. Journal of Molecular Spectroscopy 121,
694 401-409.

695 Walrafen, G.E. (1964) Raman spectral studies of water structure. Journal of
696 Chemical Physics 40, 3249-3256.
697 Walrafen, G.E., Chu, Y.C. and Carlon, H.R. (2002) Energy, Enthalpy, and Volume
698 Change of Hydrogen-Bond Formation in Large, Charged, Water Vapor Clusters,
699 $H^+(H_2O)^c$, Determined from Mass Spectral Distributions. Journal of Physical
700 Chemistry A 106, 933-937.
701 Walrafen, G.E., Fisher, M.R., Hokmabadi, M.S. and Yang, W.H. (1986)
702 Temperature dependence of the low- and high-frequency Raman scattering from
703 liquid water. Journal of Chemical Physics 85, 6970-6982.

704 Wones, D.R. and Eugster, H.P. (1962) Stability relations of the ferruginous biotite,
705 annite. Journal of Petrology3, 82-125.
706 Wyllie, P.J. (1984) Constraints imposed by experimental petrology on possible and
707 impossible magma sources and products. Philisophical Transactions of the
708 Royal Society London A 310, 439-456.
709
710

This is a preprint, the final version is subject to change, of the American Mineralogist (MSA)
Cite as Authors (Year) Title. American Mineralogist, in press.
(DOI will not work until issue is live.) DOI: http://dx.doi.org/10.2138/am-2015-4976CCBYNC

711 Table 1. Regression coefficients for least squares fits (x=a+b/T) in Figs. 12-14.
712
713 | Relationship, x | a | b | r^2 | ΔH (kJ/mol) |
714 |---|---|---|---|---|
715 | $\ln(X_{HCO_3} / X_{CO_3})$(Fig. 12) | -10.0±1.6 | 9723±1700 | 0.89 | 81±14 |
716 | $\ln(X_{CH_3} / X_{CH_4})^{fluid}$ (Fig. 13) | 1.4±0.8 | -1883±631 | 0.75 | 16±5 |
717 | $\ln(X_{CH_3} / X_{CH_4})^{melt}$ (Fig. 13) | 5.6±0.8 | -5933±673 | 0.96 | 50±7 |
718 | $\ln\left[\frac{(X_{CH_4} / X_{CH_3})^{fluid}}{(X_{CH_4} / X_{CH_3})^{melt}}\right]$(Fig. 14) | 4.2±0.4 | -4050±313 | 0.96 | 34±3 |
719
720

721

722 **Figure Captions**

723 Figure 1 –Photomicrograph of sample under reducing conditions while in
724 diamond cell at 675˚C and 986 MPa. The dense latticework of needle-shaped
725 crystals are MoO_2 crystals, melt occurs in spherical bubbles and fluid occurs as
726 a matrix as indicated.
727
728 Figure 2 – Relative intensity of Raman signal from standard microscope slide
729 (silicate glass) measured as a function of distance into air relative to the
730 intensity at the glass/air interface (focal plane) by using a 0.05 mm diameter
731 confocal hole (see text for more detailed description).
732
733 Figure 3 – Pressure-temperature paths of experimental data point under
734 reducing (closed circles) and oxidizing (closed squares) conditions.
735
736 Figure 4 - Photomicrograph of sample under oxidizing conditions at 725˚C and
737 1055 MPa. Dark areas are regions of aggregated Ag metal, bubbles are
738 CO_2+H_2O (+dissolved silicate), whereas silicate melt forms the matrix as
739 indicated.
740
741
742 Figure 5 – Photomicrograph of sample with melt and carbonate crystals
743 recorded under oxidizing conditions at 575˚C and 876 MPa.
744
745 Figure 6 – Example of Raman spectra of melts and fluids under oxidizing and
746 reducing conditions. Frequency indicators on the spectra are those where
747 peaks are visually observable. The numbers and letters are those that will be
748 used in the text when describing the spectral features. A. At 650˚C/1029 MPa
749 under oxidizing conditions in the frequency region where (Si,Al)-O vibrations
750 occur. B. At 675˚C and 986 MPa under reducing conditions (solid line) in the

same frequency range as (A). Also shown is a Raman spectrum of MoO_2 crystalline material recorded at ambient temperature and pressure. C. High-frequency portion (2800 -4400 cm^{-1}) of the same sample as that for which spectra are in the lower-frequency region are shown in A. Insert shows evolution of full width at half height (FWHH) of the 3550 cm^{-1} intensity maximum with temperature. D. Spectra in approximately the same frequency range as C of the same sample as in B (reducing conditions). Right insert shows expanded view of the peak near 4100 cm^{-1}. Left insert shows the same relationships as the insert in C except now from spectra recorded under reducing conditions.

Figure 7 – Difference spectrum (fluid-melt) under from spectra recorded under oxidizing conditions at 760°C/1205 MPa in the frequency region where (Si,Al)-O vibrations occur. Numbers indicate approximate frequencies of spectral features discussed in the text.

Figure 8 – Examples of curve-fitted spectra of supercritical fluid (A), Fluid (B) and Melt (C). Fluid and melt coexist at 610°C/1015 MPa, whereas the spectrum of supercritical fluid is from higher temperatures and pressures (900°C/1745 MPa). Fitted bands with numbers indicate their approximate frequencies. These bands also exist in spectra of NA10-H_2O fluid and melt from (Mysen, 2013). Shaded bands marked with letters, a, b, c, d are band assigned to vibrations in C-bearing complexes (see text for details).

Figure 9 – Examples of difference spectra obtained by subtracting a spectrum of fluid with that of coexisting melt at temperatures and pressures indicated.

Figure 10 – Examples of curve-fitted spectra from fluid, melt, and supercritical fluid under conditions indicated on individual panels recorded and reducing conditions in the 2800-3000 cm^{-1} frequency region.

Figure 11 – Portion of a ^{13}C MAS NMR spectrum of quenched melt in the Na-silicate system equilibrated with CH_4-H_2O-H_2 fluid at 1400°C and 1.5 GPa at the hydrogen fugacity, f_{H2}, controlled by the magnetite-wüstite buffer ($3FeO+H_2O=Fe_3O_4+H_2$) based on data from (Mysen *et al.*, 2011). The identification of one peak to molecular CH_4 and the other to CH_3 was aided by ^1H-^{13}C CPMAS measurements (Mysen *et al.*, 2011).

Figure 12 – Evolution of abundance ratio X_{HCO3}/X_{CO3} from spectra recorded under oxidizing conditions as described in text in fluids and supercritical fluids as a function of 1/T (K^{-1}) with corresponding pressures shown on the upper horizontal axis. Regression coefficients are given in Table 1.

Figure 12 – Evolution abundance ratio X_{CH3}/X_{CH4} from spectra recorded under reducing conditions as a function of 1/T (K^{-1}) with corresponding pressures shown on the upper horizontal axis. Regression coefficients are given in Table 1.

Figure 13 – Evolution of equilibrium exchange coefficient [eqn (4a)], $(X_{CH4}/X_{CH3})^{fluid}/(X_{CH4}/X_{CH3})^{melt}$, from spectra recorded under reducing conditions as described in text in fluids and supercritical fluids as a function of 1/T (K^{-1}) with corresponding pressures shown on the upper horizontal axis. Regression coefficients are given in Table 1.

Figure 15 – Change in viscosity, $\Delta\eta$, by using the fit to the viscosity in the insert in combination with equations (7a) and (7b). Changes are calculated as % of value for (C-O-H)-free melt composition with volatile-free (wo/COH) NBO/T-values equal to 0.5.

Figure 16 – Change olivine/melt exchange equilibrium coefficient, ΔK_D (= $K^{olivine/melt}_{D(Fe^{2+}-Mg)}$), by using the fit to the NBO/T-dependent coefficients in the insert

This is a preprint, the final version is subject to change, of the American Mineralogist (MSA)
Cite as Authors (Year) Title. American Mineralogist, in press.
(DOI will not work until issue is live.) DOI: http://dx.doi.org/10.2138/am-2015-4976CCBYNC

812 in combination with equations (7a) and (7b). Changes are calculated as % of
813 value for (C-O-H)-free melt composition with volatile-free (wo/COH) NBO/T-
814 values of 0.25 and 2.25. NBO/T-values near 0.3 correspond to andesite to
815 dacite composition melts, whereas NBO/T=2.25 is typical of that of peridotitic
816 komatiite.
817

This is a preprint, the final version is subject to change, of the American Mineralogist (MSA)
Cite as Authors (Year) Title. American Mineralogist, in press.
(DOI will not work until issue is live.) DOI: http://dx.doi.org/10.2138/am-2015-4976CCBYNC

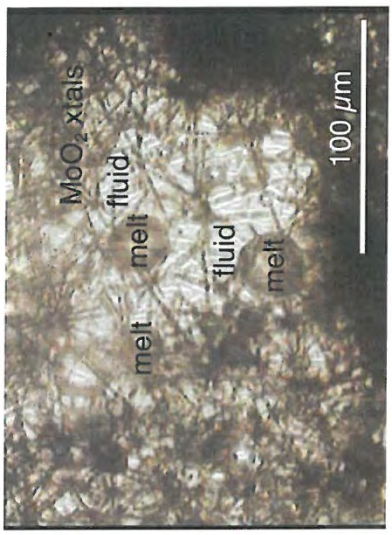

Fig. 1

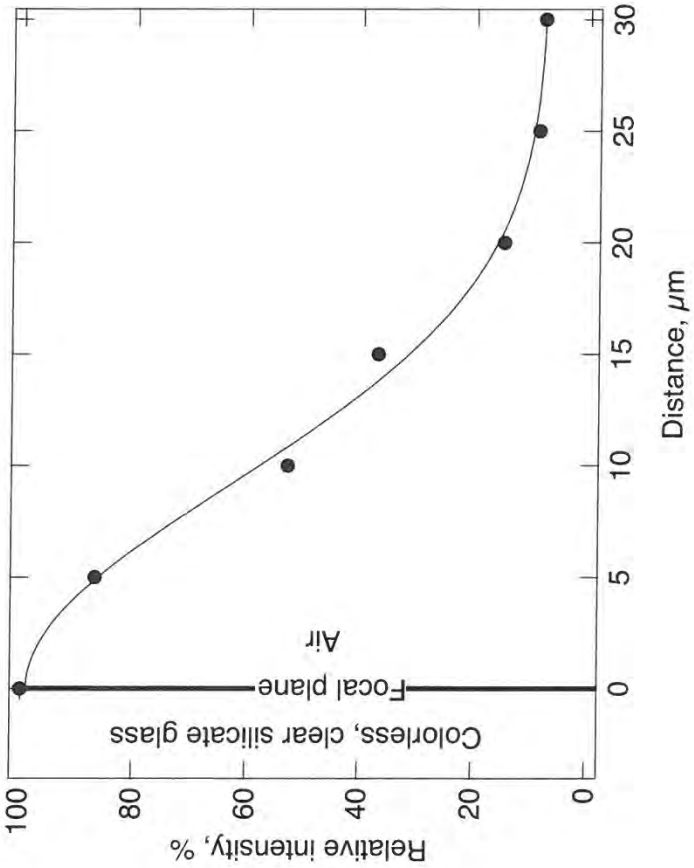
Relative intensity, %
0
20
40
60
80
100
Colorless, clear silicate glass
Focal plane
Air
0
5
10
15
20
25
30
Distance, μm

Fig. 2

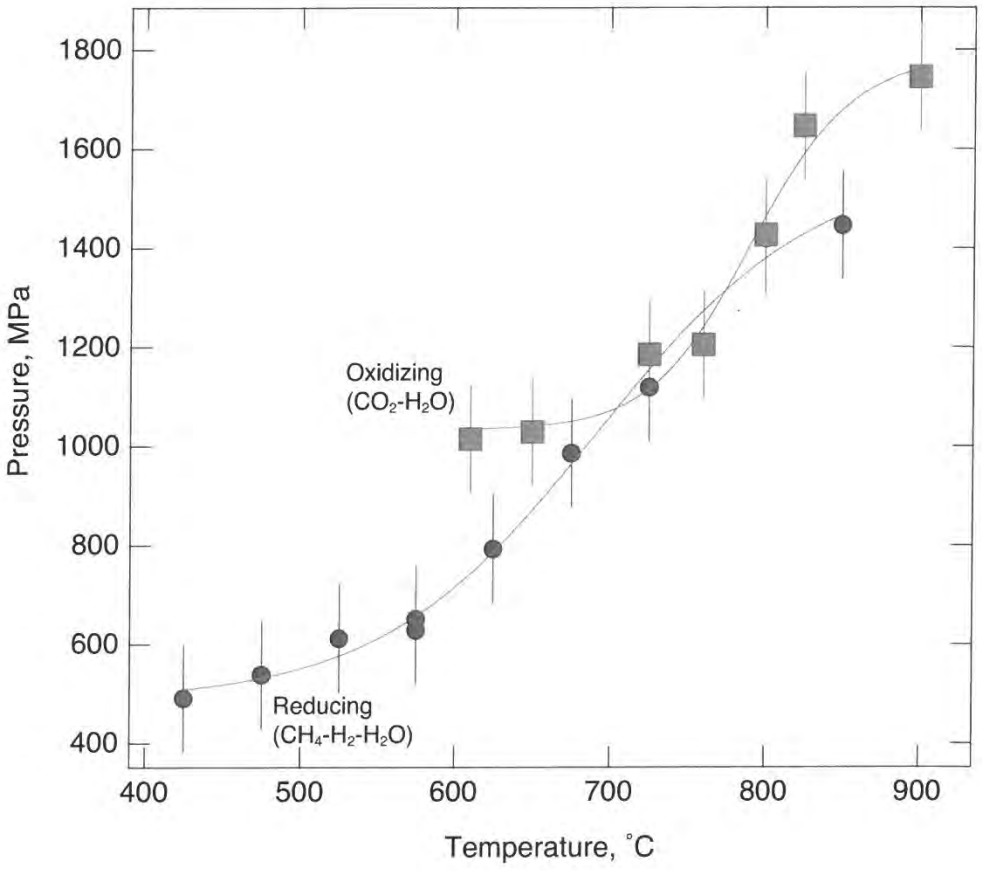
1800
1600
1400
1200
1000
800
600
400
Pressure, MPa
Oxidizing
(CO_2-H_2O)
Reducing
(CH_4-H_2-H_2O)
400
500
600
700
800
900
Temperature, ˚C

Fig. 3

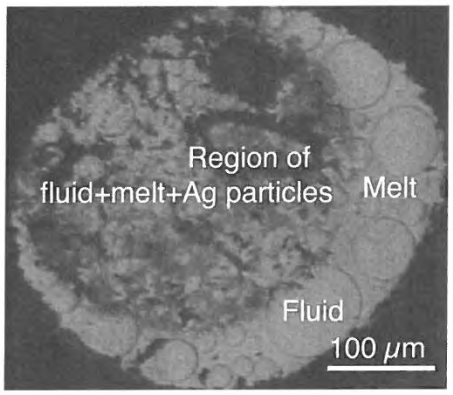

Fig. 4

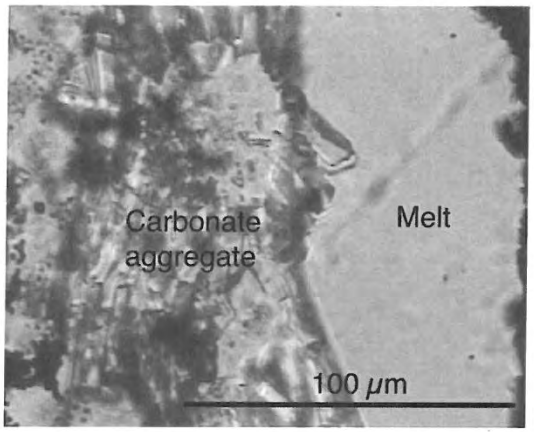

Fig. 5

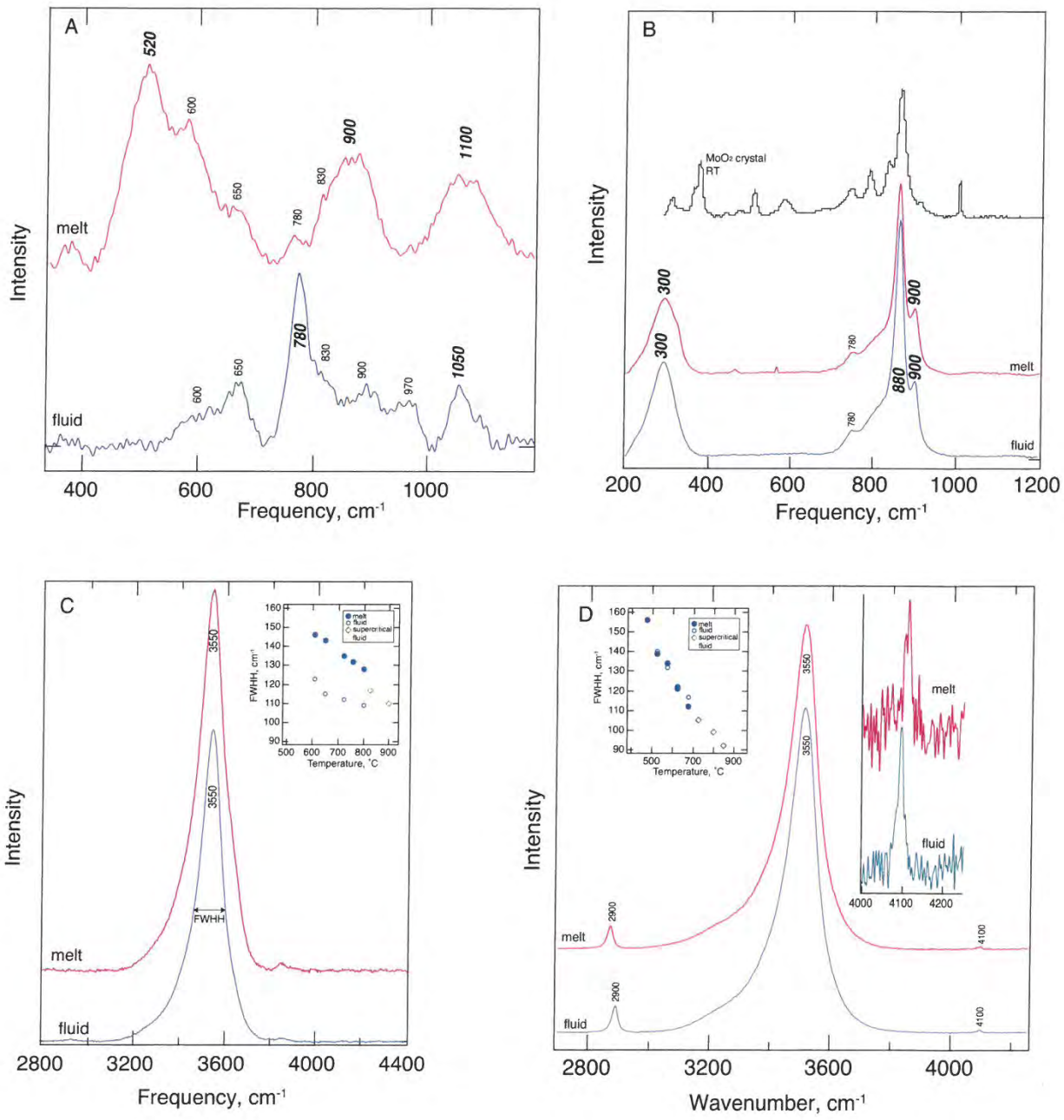
A
520
600
650
780
830
900
1100
melt
fluid
600
650
780
830
900
970
1050
Intensity
400
600
800
1000
Frequency, cm-1
B
MoO2 crystal
RT
300
300
780
900
900
880
780
melt
fluid
Intensity
200
400
600
800
1000
1200
Frequency, cm-1
C
3550
3550
FWHH
melt
fluid
Intensity
melt
fluid
supercritical fluid
FWHH, cm-1
Temperature, °C
2800
3200
3600
4000
4400
Frequency, cm-1
D
3550
3550
melt
fluid
2900
2900
4100
4100
melt
fluid
Intensity
melt
fluid
supercritical fluid
FWHH, cm-1
Temperature, °C
4000
4100
4200
2800
3200
3600
4000
Wavenumber, cm-1

Fig. 6

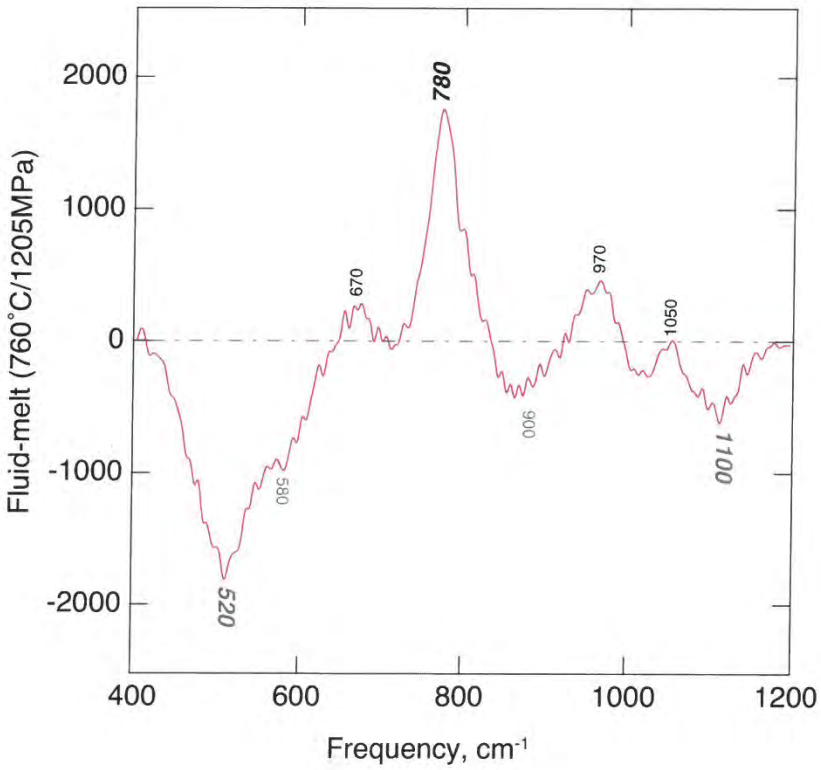
2000
1000
0
-1000
-2000
Fluid-melt (760°C/1205MPa)
400
600
800
1000
1200
Frequency, cm-1
520
580
670
780
900
970
1050
1100

Fig. 7

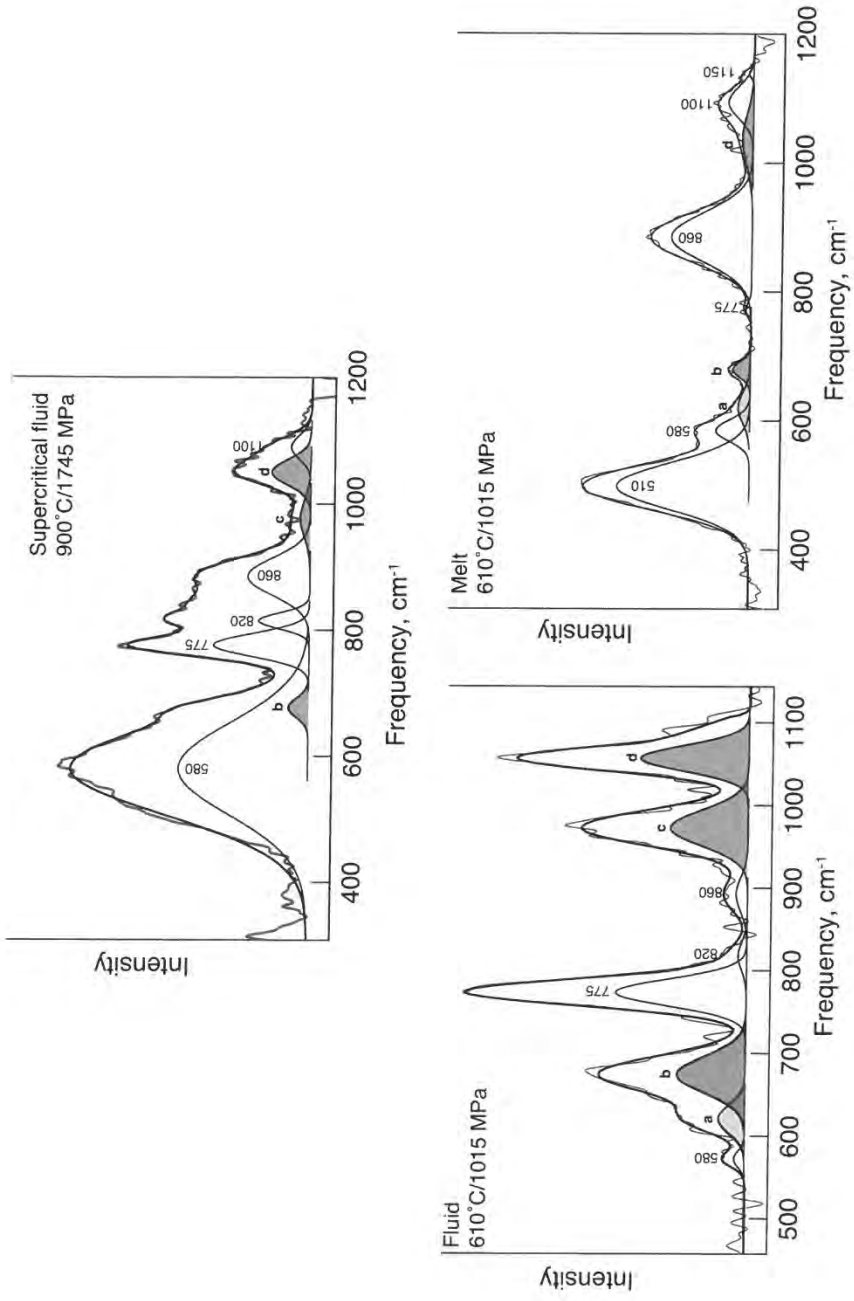
Supercritical fluid
900°C/1745 MPa
Melt
610°C/1015 MPa
Fluid
610°C/1015 MPa
Intensity
Frequency, cm-1
580
510
775
820
860
1100
1150
a
b
c
d

Fig. 8

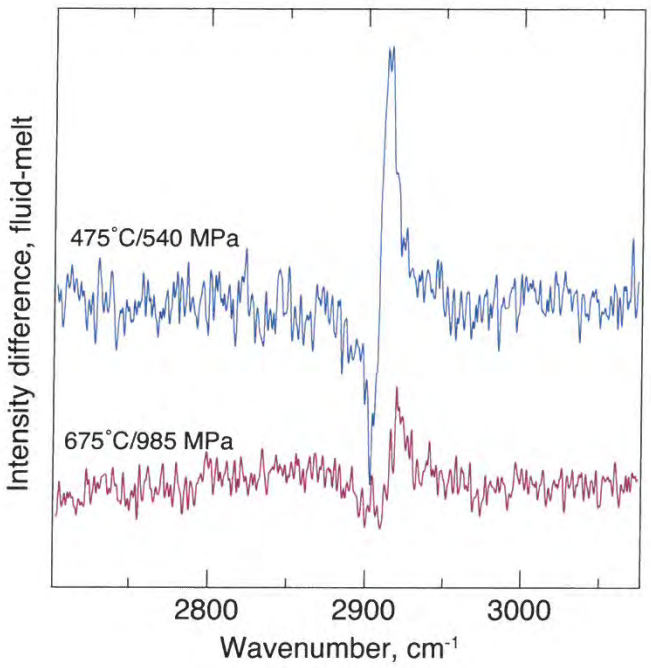
Intensity difference, fluid-melt
475°C/540 MPa
675°C/985 MPa
2800
2900
3000
Wavenumber, cm-1

Fig. 9

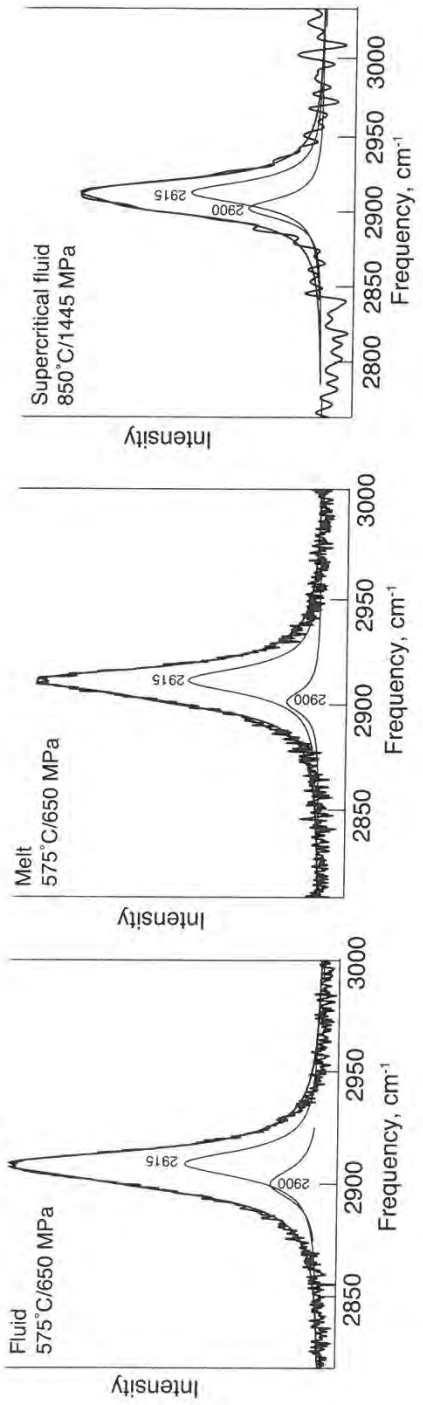
Supercritical fluid
850°C/1445 MPa
Intensity
2915
2900
2800
2850
2900
2950
3000
Frequency, cm-1
Melt
575°C/650 MPa
Intensity
2915
2900
2850
2900
2950
3000
Frequency, cm-1
Fluid
575°C/650 MPa
Intensity
2915
2900
2850
2900
2950
3000
Frequency, cm-1

Fig. 10

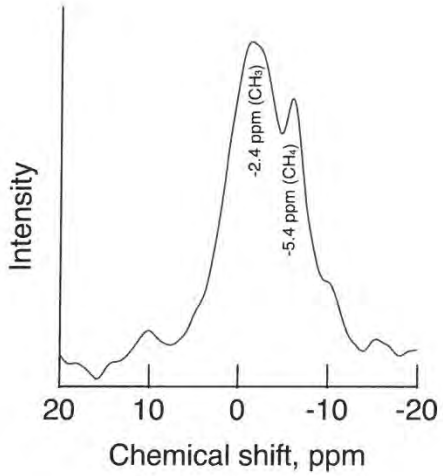
Intensity
-2.4 ppm (CH_3)
-5.4 ppm (CH_4)
20
10
0
-10
-20
Chemical shift, ppm

Fig. 11

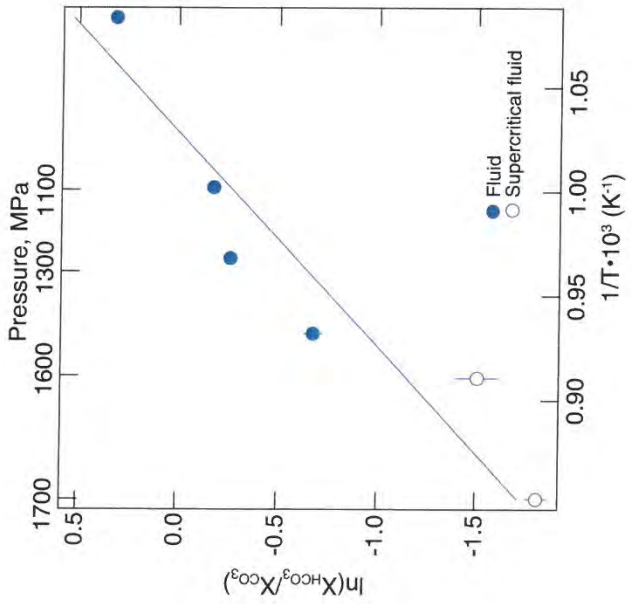
Pressure, MPa
1700
1600
1300
1100
0.5
0.0
-0.5
-1.0
-1.5
ln(X$_{HCO_3}$/X$_{CO_3}$)
0.90
0.95
1.00
1.05
1/T•10^3 (K^{-1})
Fluid
Supercritical fluid

Fig. 12

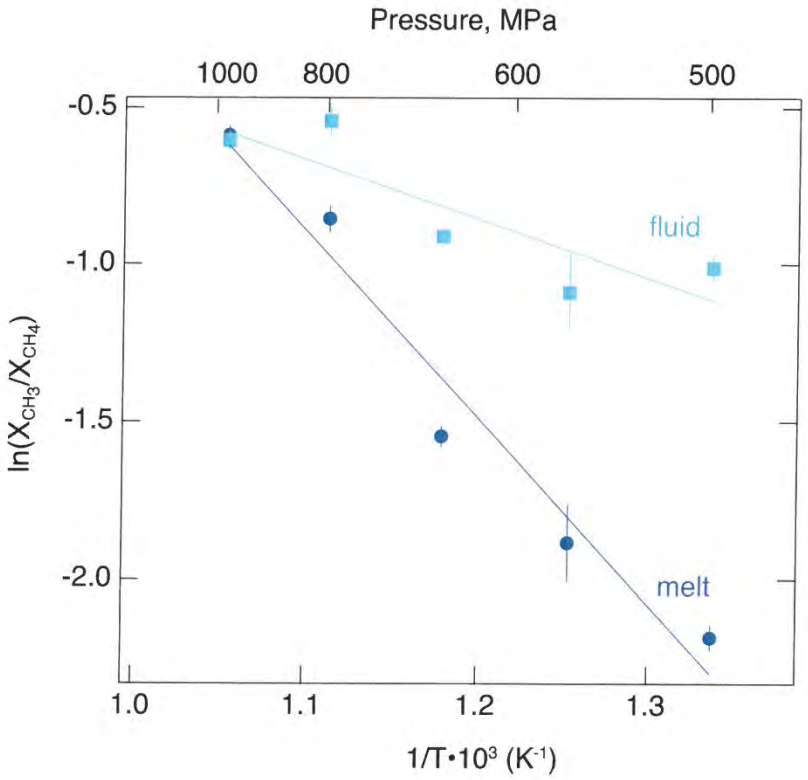
Pressure, MPa
1000
800
600
500
-0.5
-1.0
-1.5
-2.0
fluid
melt
ln(X_CH3/X_CH4)
1.0
1.1
1.2
1.3
1/T•10³ (K⁻¹)

Fig. 13

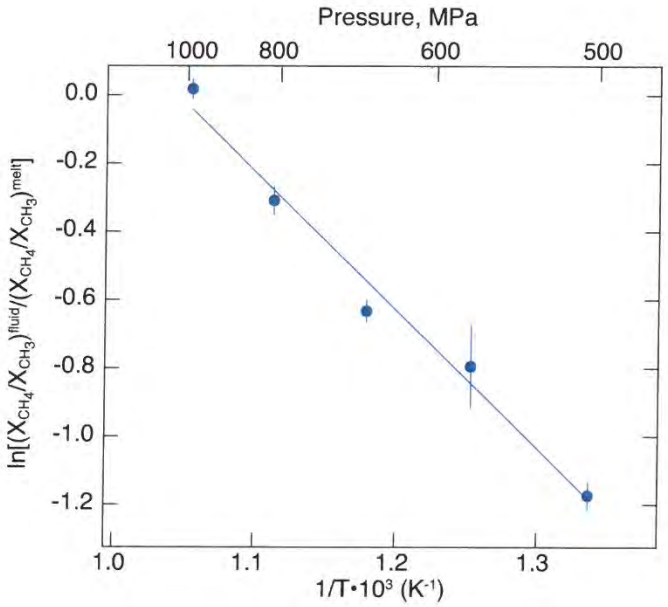
Pressure, MPa
1000
800
600
500
0.0
-0.2
-0.4
-0.6
-0.8
-1.0
-1.2
ln[(X_CH4/X_CH3)^fluid/(X_CH4/X_CH3)^melt]
1.0
1.1
1.2
1.3
1/T•10³ (K⁻¹)

Fig. 14

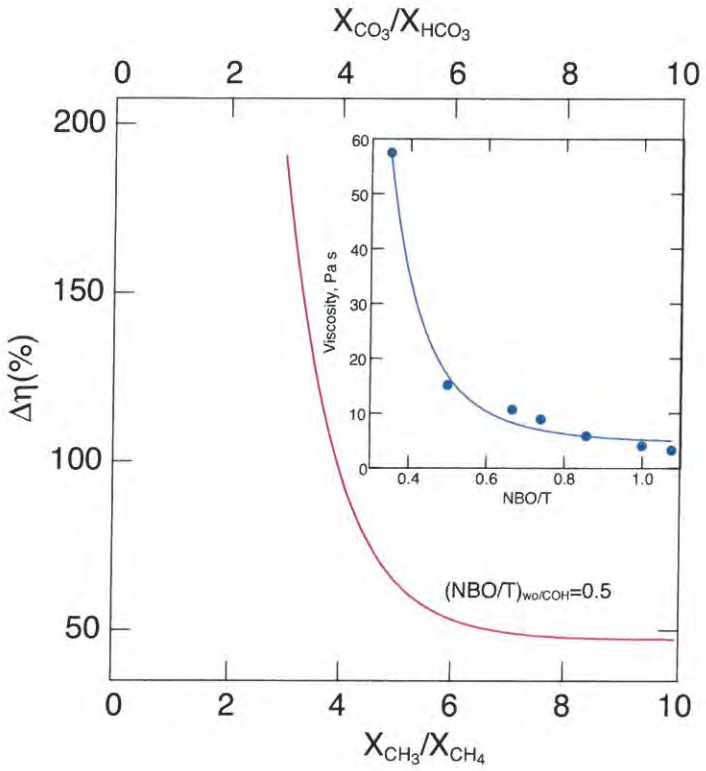
X_{CO_3}/X_{HCO_3}
0
2
4
6
8
10
200
150
100
50
Δη(%)
60
50
40
30
20
10
0
Viscosity, Pa s
0.4
0.6
0.8
1.0
NBO/T
$(NBO/T)_{wo/COH}$=0.5
X_{CH_3}/X_{CH_4}

Fig. 15

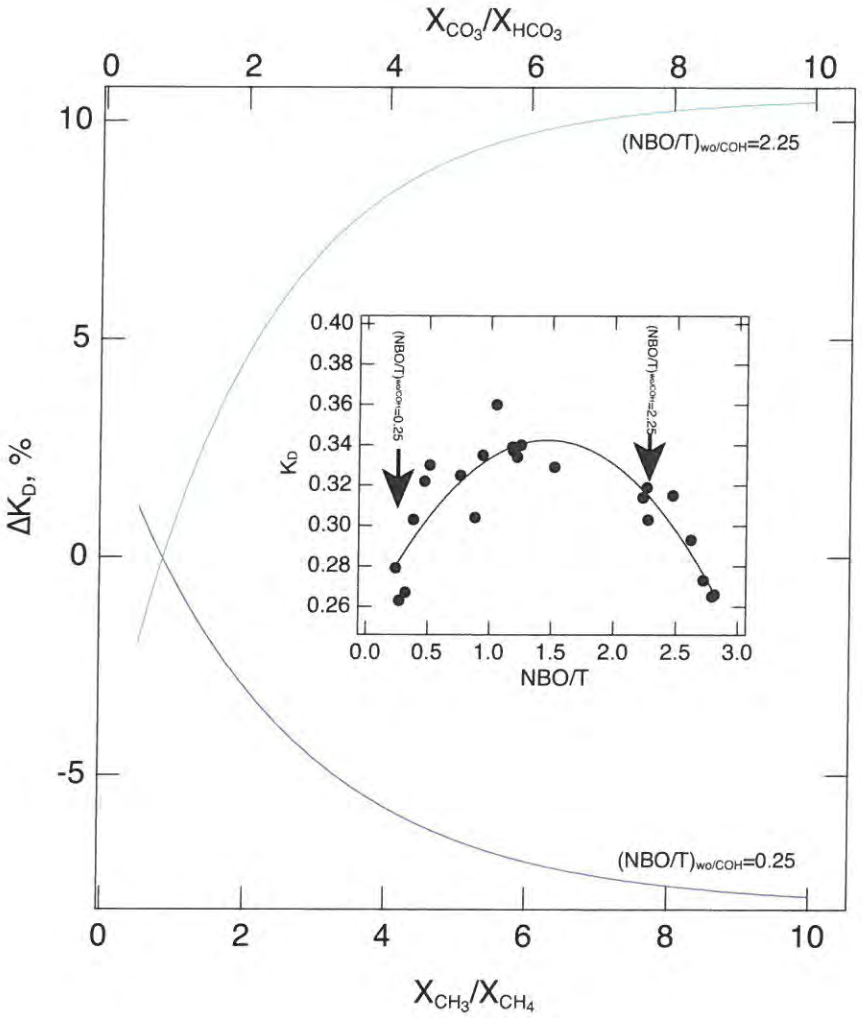
X_{CO_3}/X_{HCO_3}
0
2
4
6
8
10
10
5
0
-5
ΔK_D, %
$(NBO/T)_{wo/COH}$=2.25
$(NBO/T)_{wo/COH}$=0.25
X_{CH_3}/X_{CH_4}
K_D
0.40
0.38
0.36
0.34
0.32
0.30
0.28
0.26
0.0
0.5
1.0
1.5
2.0
2.5
3.0
NBO/T
$(NBO/T)_{wo/COH}$=0.25
$(NBO/T)_{wo/COH}$=2.25

Fig. 16